

# SPATIAL FUNCTA: SCALING FUNCTA TO IMAGENET CLASSIFICATION AND GENERATION

Matthias Bauer\*<sup>1</sup> Emilien Dupont<sup>1</sup> Andy Brock<sup>1</sup> Dan Rosenbaum<sup>2</sup> Jonathan Schwarz<sup>1</sup>  
Hyunjik Kim\*<sup>1</sup>

<sup>1</sup>DeepMind, <sup>2</sup>University of Haifa

## ABSTRACT

Neural fields, also known as implicit neural representations, have emerged as a powerful means to represent complex signals of various modalities. Based on this Dupont et al. (2022a) introduce a framework that views neural fields as data, termed *functa*, and proposes to do deep learning directly on this dataset of neural fields. In this work, we show that the proposed framework faces limitations when scaling up to even moderately complex datasets such as CIFAR-10. We then propose *spatial functa*, which overcome these limitations by using spatially arranged latent representations of neural fields, thereby allowing us to scale up the approach to ImageNet-1k at  $256 \times 256$  resolution. We demonstrate competitive performance to Vision Transformers (Steiner et al., 2022) on classification and Latent Diffusion (Rombach et al., 2022) on image generation respectively.

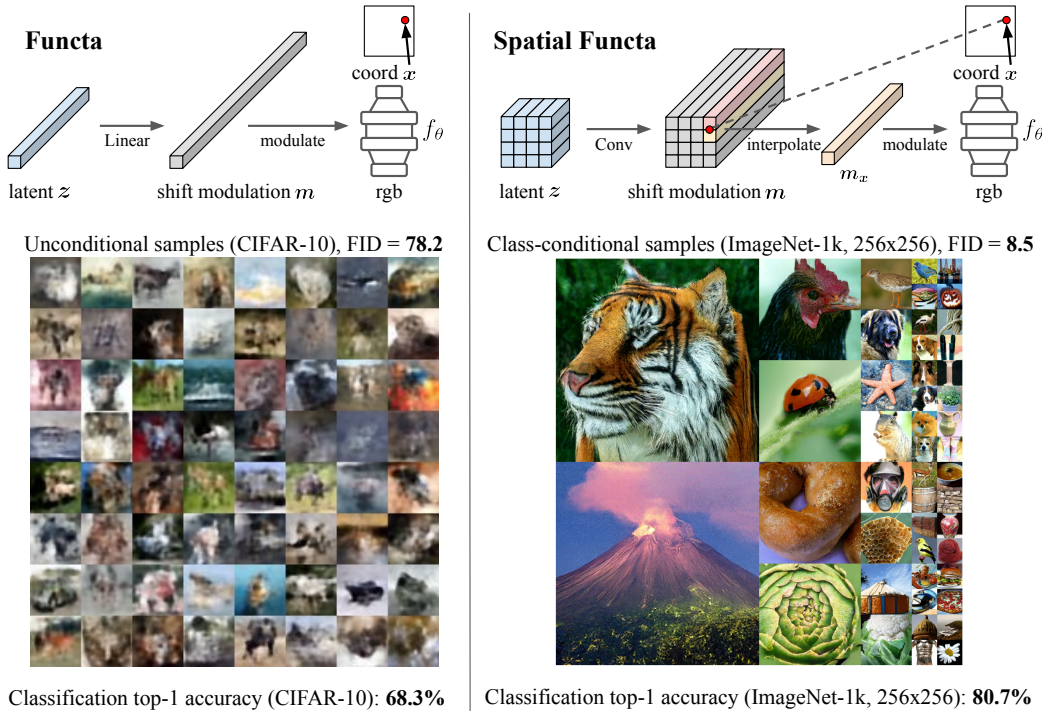


Figure 1: Comparing *functa* (Dupont et al., 2022a) to our proposed *spatial functa*. *Top row*: neural field parameterizations. *Bottom row*: curated samples and classification accuracies on CIFAR-10 (*functa*) and ImageNet  $256 \times 256$  (*spatial functa*), respectively, without pretraining on other datasets.

\*Equal Contribution. Correspondence to: {hyunjikk, msbauer}@google.com.

---

## 1 INTRODUCTION

*Neural fields*, also known as *implicit neural representations* (INRs), are coordinate-based neural networks that represent a field, such as a 3D scene, by mapping 3D coordinates to colour and density values in 3D space. Neural fields have recently gained significant traction in computer vision as a method to represent signals such as images (Ha, 2016), 3D shapes/scenes (Park et al., 2019; Mescheder et al., 2019; Mildenhall et al., 2020), video (Chen et al., 2021a), audio (Sitzmann et al., 2020), medical images (Shen et al., 2022) and climate data (Dupont et al., 2021b). Building on the fact that neural fields can represent signals in such a wide range of modalities, Dupont et al. (2022a) recently proposed a framework termed *functa* for doing deep learning directly on these field representations, rather than the classical approach of processing array representations such as pixels. They show promising results on generation, inference and classification across a wide range of modalities. They cover images, voxels, climate data and 3D scenes, but on fairly small scale and simple datasets e.g. CelebA-HQ  $64 \times 64$  (Karras et al., 2018), ShapeNet (Chang et al., 2015).

In this work, we propose a method for scaling up *functa* to larger and more complex datasets. Concretely, we make the following contributions:

- After reproducing the reported *functa* results on CelebA-HQ, we apply the same methodology to downstream tasks on CIFAR-10, and show that – surprisingly – the results on classification and generation are far below expectations (see left of Fig. 1 and Tab. 1).
- We introduce *spatial functa*, a spatially arranged representation of *functa* whose features capture local signal information in input space.
- We demonstrate that *spatial functa* overcome the limitations observed for CIFAR-10 classification/generation and can scale to much larger datasets, namely ImageNet-1k at  $256 \times 256$  resolution. This is demonstrated by classification results that are competitive with ViTs (Steiner et al., 2022) and image generation results competitive with Latent Diffusion (Rombach et al., 2022).

## 2 BACKGROUND ON NEURAL FIELDS AND FUNCTA

**Neural fields** are functions  $f_\theta$  mapping *coordinates*  $x$  (e.g. pixel locations) to *features*  $f$  (e.g. RGB values) parameterized by  $\theta$ . They are fit to a particular signal by minimizing the reconstruction loss between the output  $f$  and the target signal value at all available coordinates  $x$ . For example, an image would correspond to a single  $f_\theta$ , usually an MLP with sinusoidal activation functions, i.e., a SIREN (Sitzmann et al., 2020). Neural fields are very general and can represent a wide range of the aforementioned modalities.

**Functa** (Dupont et al., 2022a) is a framework that treats neural fields as data points, elements of a *functaset*, on which we can perform deep learning tasks. See App. A for a more thorough introduction. The motivations for doing so include: (1) **better scaling** of data dimensionality compared to array representations, leading to more memory/compute efficient training of neural networks for downstream tasks; (2) **moving away from a fixed resolution**; (3) allowing for **unified frameworks and architectures across multiple data modalities**; (4) dealing with **signals that are inherently difficult to discretize**, such as fields on non-Euclidean manifolds, e.g., climate data. Dupont et al. (2022a) show promising results on relatively small scale datasets with limited complexity. In this work we ask the question: *does the approach scale to more complex / larger datasets? If not, how can we make it scale?*

## 3 LIMITATIONS OF NAIVELY SCALING UP FUNCTA

Following implementation details by Dupont et al. (2022a), we were able to reproduce reported results on CelebA-HQ ( $64 \times 64$ ) and subsequently applied *functa* to CIFAR-10 ( $32 \times 32$ ). We discovered that, while the meta-learned *functa* latent representations could faithfully reconstruct the data, on downstream tasks they significantly underperformed pixel-based classification and generation.

More specifically, we were able to fit each CIFAR-10 image successfully with meta-learning, that is, we could reconstruct test set images to very high fidelity (38.1dB peak signal to noise ratio (PSNR))

on the test set with 1024 dimensional latents, see Tab. 1)<sup>1</sup>. Hence it is clear that the information necessary for downstream tasks is still present in the latent representation. However, we found that both MLPs (with residual connections as successfully employed by Dupont et al. (2022a) on simpler datasets) and Transformers struggle to make use of this information for downstream tasks: Starting from the model configurations and insights by Dupont et al. (2022a), we carried out a thorough hyperparameter search across architectures for both classification and generation using DDPM (Ho et al., 2020). We varied model sizes, optimizer configurations and explored standard regularization techniques such as data augmentation, model averaging and label smoothing (for classification) to push performance. However the best top-1 accuracy that we were able to achieve was 68.3%, and the best FID for diffusion modeling was 78.2, c.f. samples in Fig. 1 (left). See App. B for details.

It is surprising that functa underperforms on both downstream tasks on CIFAR-10 given that Dupont et al. (2022a) report competitive results on ShapeNet voxel classification and generation using relatively simple (MLP) architectures.

latent dim	Test PSNR	top-1 acc	FID (uncond)
256	27.6 dB	66.7%	<b>78.2</b>
512	31.9 dB	<b>68.3%</b>	96.1
1024	<b>38.1 dB</b>	66.7%	134.8

Table 1: CIFAR-10 functa results

One key property of functa latent representations is that they encode data as one global vector; i.e., each latent dimension encodes global features that span the entire image/data point when viewed in pixel space. We demonstrate this via a perturbation analysis on CIFAR-10, where changes in any latent dimension lead to global perturbations across the reconstructed image in pixel space, c.f. Fig. 4, App. B. In contrast, in the data domain information is naturally spatially arranged and localized; indeed, architectures such as convolutional networks on pixel/voxel arrays or Transformers on spatio-temporal arrays explicitly exploit this spatial structure.

We hypothesize that the stark performance differences between functa on CelebA / ShapeNet and CIFAR-10 arise due to differing complexities of the tasks at hand. For sufficiently simple tasks, architectures such as MLPs and Transformers are able to extract features that are useful for these tasks from global latent representations of the underlying neural field. For more challenging tasks however, they struggle to extract sufficiently expressive features. This naturally motivates us to explore *spatial functa* latent representations of functa, which we call *spatial functa*.

## 4 SPATIAL FUNCTA

Here we present *spatial functa*, a generalization of functa that uses spatially arranged latent representations instead of flat latent vectors. This allows features at each spatial index to capture local information as opposed to global information spread across all spatial locations. This simple change enables us to solve downstream tasks with more powerful architectures such as Transformers with positional encodings (Vaswani et al., 2017) and UNets (Ronneberger et al., 2015), whose inductive biases are suitable for spatially arranged data. In Sec. 5 we show that this greatly improves the usefulness of representations extracted from functa latents for downstream tasks, allowing the functa framework to scale to complex datasets such as ImageNet-1k at  $256 \times 256$  resolution.

*Functa* linearly map the (global) latent vector to a vector of shift modulations, which is subsequently used to condition the neural field at all positions  $x$ , see Fig. 1 (top left). Shift modulations are bias terms that get added to the activations at each layer the MLP neural field  $f_\theta$ . In *spatial functa* we still use a vector of shift modulations to condition the neural field for each position  $x$ , however, the modulation vector  $m_x$  is now position dependent. To achieve this, we first linearly map the spatial latent  $z \in \mathbb{R}^{s \times s \times c}$  to a spatially arranged shift modulation  $m \in \mathbb{R}^{s \times s \times C}$  using a single convolutional layer  $m = \lambda(z)$ , where  $s < d$ , the image resolution. From the spatial shift modulation  $m$  we then extract the position-dependent modulation vector  $m_x \in \mathbb{R}^C$  by interpolation, see Fig. 1 (top right). The pixel value output of the neural field  $f_\theta$  queried at position  $x$  is then given by  $f_\theta(x; m_x)$ .

The modulations  $m_x$  are constrained to depend only on latent features that correspond to the coordinate of interest  $x$ , in order to enforce the property that  $z$  encodes local information in space. We focus on two interpolation schemes: (a) *nearest neighbor* – modulation vector is constant over

<sup>1</sup>This PSNR value corresponds to a mean absolute error of  $\approx 3$  units per RGB value (units in range  $[0, 255]$ ), which is hardly noticeable to the human eye, see Fig. 3, App. B

patches in coordinate space; and (b) *bilinear interpolation* of the  $s \times s$  spatial features to obtain  $m_x$ . Using nearest neighbor interpolation (with  $\lambda$  a  $1 \times 1$  convolution) for grid data, such as images at  $d \times d$  resolution, means that we have an independent  $c$ -dimensional latent feature per patch of size  $d/s \times d/s$ . Also note that we recover the original functa parameterization by setting  $s = 1$ .

With the above parameterization of each data point as a spatial functa point, we train all parameters and build a (spatial) functaset exactly like Dupont et al. (2022a) via meta-learning: we learn the parameters shared across all data points, namely the latent-to-modulation linear map  $\lambda$  and the weights  $\theta$  for the neural field  $f_\theta$ . After training, we freeze  $\lambda$  and  $\theta$  and create a functaset by converting each data point to a spatial latent  $z$  via 3 gradient steps from a zero initialization. We then use the spatial functaset  $\{z^{(i)}\}_i$ , with each data point represented by a latent  $z^{(i)}$  as input data for downstream tasks.

## 5 EXPERIMENTAL RESULTS

In the following we train and build spatial functasets for CIFAR-10 and ImageNet256 with differing latent shapes and interpolations. To assess their quality, we first report reconstruction PSNRs on the respective test sets. We then train classifiers and generative models on these functasets, evaluating performance via: (a) top-1 classification test accuracies using Transformer classifiers; and (b) FID scores using convolutional UNet-based diffusion models.

### 5.1 CIFAR-10 CLASSIFICATION AND GENERATION WITH SPATIAL FUNCTA

Latent shape	Interpolation	Test PSNR $\uparrow$	Top-1 acc $\uparrow$	FID (uncond) $\downarrow$	FID (cond) $\downarrow$
$8 \times 8 \times 16$	1-NN	37.2 dB	<b>90.3%</b>	<b>16.5</b>	11.2*
$8 \times 8 \times 16$	Linear	35.6 dB	83.0%	25.6	11.6*
$4 \times 4 \times 64$	1-NN	<b>39.0</b> dB	88.2%	44.6	<b>10.4*</b>
$4 \times 4 \times 64$	Linear	35.3 dB	80.8%	71.2	11.0*

Table 2: CIFAR-10 spatial functa results. \*Model memorizes subset of training set. Details in C.2.

We first revisit CIFAR-10 to show that spatial functa overcome the limitations discussed in Sec. 3. Instead of a single feature vector, we use a grid of smaller feature vectors such that the overall dimensionality of the latent stays the same (1024 dims). See App. C.1 for model and training details.

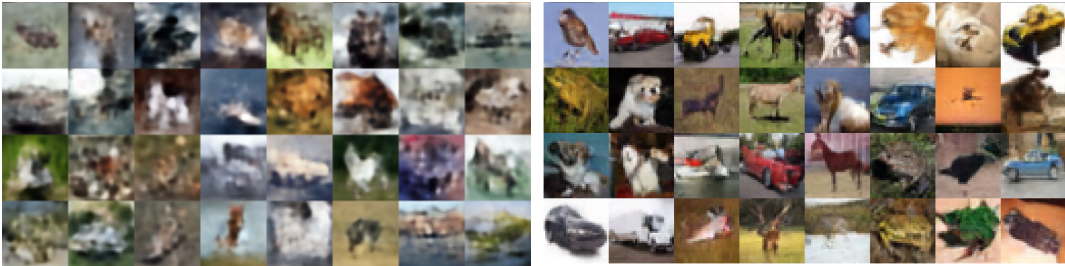


Figure 2: Uncurated samples from unconditional DDPM with best FID score. *left*: original vector-valued functa, FID = 78.2; *right*: spatial functa, FID = 16.5.

On both tasks, spatial functa perform markedly better than the original vector-valued functa despite their similar reconstruction PSNR: For classification we now achieve a top-1 accuracy of 90.3% (see Tab. 2) instead of 68.3% (see Tab. 1). Similar improvements can be observed for image generation with Latent Diffusion: we achieve FIDs of 16.5 (with an unconditional model without classifier-free guidance) and 10.4 (with a conditional model with classifier-free guidance) for spatial functa (see Tab. 2) compared to 134.8 for functa with the same latent dimensionality and 78.2 with fewer latent dimensions (see Tab. 1). In Fig. 2 we contrast uncurated samples of vector-valued and spatial functa.

In general, nearest neighbor interpolation tends to perform better than linear interpolation for downstream tasks. In both reconstructions and samples we do not observe patch artifacts, likely because

the reconstruction PSNR is high enough, so the diffusion model learns to generate samples that match up on the patch boundaries. Moreover, the higher the spatial latent dimensionality (while keeping total number of latent dimensions fixed), the better the performance on both downstream tasks. This observation indicates the importance of locality for extracting useful features in downstream tasks through Transformers and UNets.

Similar to [Nichol & Dhariwal \(2021\)](#) we observed that class-conditional diffusion models can easily collapse to memorizing (a subset of) the CIFAR-10 training set. We discuss this overfitting and our solution – using unconditional DDPM on the dataset instead – in [App. C.2](#).

## 5.2 IMAGENET $256 \times 256$ CLASSIFICATION AND GENERATION WITH SPATIAL FUNCTA

We repeat similar experiments on ImageNet-1k  $256 \times 256$ . We again found that nearest neighbor interpolation always gave better performance and that larger spatial dimensions of the latents yielded the best PSNR, which also correlates with best top-1 accuracy and best FID scores, see [Tab. 3](#). See [C.3](#) for further results and details on architectures and hyperparameters for these downstream tasks.

Model	Input shape	Test PSNR $\uparrow$	Top-1 acc $\uparrow$	FID (cond) $\downarrow$
Spatial Functa (1-NN)	$8 \times 8 \times 256$	28.3dB	76.6%	17.9
	$8 \times 8 \times 512$	30.6dB	76.5%	23.5
	$8 \times 8 \times 1024$	25.7dB	76.5%	-
	$16 \times 16 \times 64$	28.9dB	80.4%	12.5
	$16 \times 16 \times 128$	37.8dB	<b>80.7%</b>	10.5
	$16 \times 16 \times 256$	37.2dB	80.6%	11.7
	$32 \times 32 \times 16$	28.6dB	-	12.4
	$32 \times 32 \times 32$	31.7dB	-	10.5
	$32 \times 32 \times 64$	37.7dB	-	8.8
	$32 \times 32 \times 64^*$	<b>38.4 dB</b>	-	<b>8.5</b>
ViT-B/16	$224 \times 224 \times 3$	-	79.8%	-
	$384 \times 384 \times 3$	-	<b>81.6%</b>	-
LDM-8-G	$32 \times 32 \times 4$ (14 bits)	23.1dB	-	7.8
LDM-4-G	$64 \times 64 \times 3$ (13 bits)	27.4dB	-	<b>3.6</b>

Table 3: ImageNet classification and diffusion results. \*Indicates that a  $3 \times 3$  Conv was used instead of  $1 \times 1$  Conv for the latent to modulation linear map.

For classification, there is little difference across different numbers of feature dimensions. Note that we omit classification results for  $32 \times 32$  latent dimensions as this would correspond to a sequence length of 1024 for the Transformer classifier, which makes the vanilla Transformer too costly in terms of memory. For a similar reason ViT on ImageNet only explores patch sizes  $\geq 32$  ([Dosovitskiy et al., 2021](#); [Steiner et al., 2022](#)). We also omit diffusion results for latent shape  $8 \times 8 \times 1024$  as DDPM suffered from training instabilities.

Our best classification performance using spatial functa is 80.7% on  $16 \times 16 \times 128$  latent dimensions, which is competitive with ViT-B/16, the best performing Vision Transformer at patch-size 16 (i.e., using the same sequence length of 256 as our best performing Transformer) trained on the same ImageNet-1k dataset with similar data augmentation<sup>2</sup> ([Steiner et al., 2022](#)). Note that the numbers for ViT are for two different resolutions  $224 \times 224$  and  $384 \times 384$ ; our resolution of  $256 \times 256$  is closer to the former yet has better accuracy. Moreover our classifier has 64M parameters compared to 86M parameters for ViT-B/16.

For image generation, the best model achieves an FID of 8.50 (with 277M parameters); see curated samples in [Fig. 1 \(bottom right\)](#), and uncurated samples in [Fig. 6](#). This FID score is close to the best performing Latent Diffusion model with the same spatial downsampling factor: LDM-8-G at 7.76 (with 506M parameters) ([Rombach et al., 2022](#)). We expect better FID with a smaller downsampling factor, just as LDM-4-G (3.60) is better than LDM-8-G (7.76).

<sup>2</sup>ViT actually uses stronger augmentations, RandAugment and MixUp, whereas we only use RandAugment

---

### 5.3 ABLATIONS

Besides model size and latent shape, several other hyperparameters affect model performance, in particular for image generation. These include the normalization of the functaset, the guidance scale for classifier-free guidance, and the sampling of timesteps for diffusion training. We discuss these ablations as well as preliminary results for compression of the spatial functa via quantization in C.4.

## 6 RELATED WORK

Here we focus on works that are relevant to spatial functa or date after Dupont et al. (2022a). Please refer to their related work section for references on functa that precede it.

Modeling neural fields with spatial latent features has become popular across a wide range of modalities. Grounding outputs of neural fields on spatial latents (with or without interpolation) has been shown to allow for efficient fitting and inference of neural fields at high fidelity in modalities such as 3D scenes/shapes (Jiang et al., 2020; Chabra et al., 2020; Chibane et al., 2020; Fridovich-Keil et al., 2022; Müller et al., 2022; Chen et al., 2022), videos (Kim et al., 2022) and images (Mehta et al., 2021; Chen et al., 2021b). We show that such spatial representations of neural fields are also particularly important for deep learning on neural fields to solve both discriminative (e.g. classification) and generative (e.g. synthesis) downstream tasks at scale. Although we demonstrate this only on image datasets (up to ImageNet-1k at  $256 \times 256$  scale), we expect this observation to also hold more generally for sufficiently complex datasets of other modalities.

Two recent works further exemplify the importance of spatial latents for generative modeling. Using diffusion they successfully model 3D shapes (Shue et al., 2022) and scenes (Bautista et al., 2022) and crucially rely on spatial representations and a functa-like framework that consists of two decoupled stages: 1. creation of a dataset of neural fields and 2. subsequent downstream learning on this dataset. Both works focus on generative downstream tasks with diffusion models and on datasets with a small number of data points ( $\leq 10k$  shapes/scenes). In contrast, our work evaluates on both generative *and* discriminative tasks and uses datasets with  $> 1M$  data points (ImageNet).

Concurrently, Luigi et al. (2023) employ the functa framework for 3D shapes, namely treating each shape as a neural field, and do not rely on spatial latent features, rather a single latent vector representation per shape. The key difference is that they use an encoder to map the weights and biases of each SIREN field to the latent representation, whereas in functa the encoding is done by gradient updates. These latents are shown to be useful for various downstream tasks such as point cloud retrieval, classification, generation and segmentation. However the approach has only been applied to ShapeNet, where the original functa methodology was also shown to perform well on downstream tasks, so it remains to be seen whether their proposed methodology can be extended to CIFAR-10 and ImageNet scale.

Several recent works propose continuous kernel convolutions (Romero et al., 2022b;a) that can process functional representations, and Wang & Golland (2022) employ such architectures for deep learning on neural fields. However as it stands, this approach does not scale to datasets beyond CIFAR-10 due to the compute/memory costs of continuous kernel convolutions.

## 7 CONCLUSION AND FUTURE WORK

In this work, we have shown that the original neural field parameterization used in *functa* (Dupont et al., 2022a) struggles to scale functa classification and generation to even relatively small datasets such as CIFAR-10. We then proposed a spatial parameterization, termed *spatial functa*, and showed that this allows for scaling functa to ImageNet-1k at  $256 \times 256$  resolution, achieving competitive classification performance with ViT (Steiner et al., 2022) and generation performance with Latent Diffusion (Rombach et al., 2022).

We emphasize that achieving competitive results on image tasks is not the ultimate goal, but rather a stepping stone for scaling up functa in other modalities such as video (+ audio) and static/dynamic scenes. We believe these higher dimensional modalities are where the functa framework will truly shine with scale, since the vast amounts of redundant information in array-representations of these modalities can be captured much more efficiently as neural fields.

---

We also highlight that while we can successfully scale functa with spatial functa, we have not fully answered the question as to why the original vector-valued functa representations are difficult to use in larger scale downstream tasks. This is an interesting open problem, and a potential avenue for exploration would be to devise efficient architectures that allow extracting useful representations from flat vector representations of functa for sufficiently complex datasets at scale.

#### ACKNOWLEDGMENTS

We thank Yee Whye Teh for helpful discussions around the project, and S. M. Ali Eslami for helpful feedback regarding the manuscript.

#### REFERENCES

- Miguel Angel Bautista, Pengsheng Guo, Samira Abnar, Walter Talbott, Alexander Toshev, Zhuoyuan Chen, Laurent Dinh, Shuangfei Zhai, Hanlin Goh, Daniel Ulbricht, et al. Gaudi: A neural architect for immersive 3d scene generation. *arXiv preprint arXiv:2207.13751*, 2022.
- Rohan Chabra, Jan E Lenssen, Eddy Ilg, Tanner Schmidt, Julian Straub, Steven Lovegrove, and Richard Newcombe. Deep local shapes: Learning local sdf priors for detailed 3d reconstruction. In *European Conference on Computer Vision*, pp. 608–625. Springer, 2020.
- Angel X Chang, Thomas Funkhouser, Leonidas Guibas, Pat Hanrahan, Qixing Huang, Zimo Li, Silvio Savarese, Manolis Savva, Shuran Song, Hao Su, et al. Shapenet: An information-rich 3d model repository. *arXiv preprint arXiv:1512.03012*, 2015.
- Anpei Chen, Zexiang Xu, Andreas Geiger, Jingyi Yu, and Hao Su. Tensorf: Tensorial radiance fields. In *European Conference on Computer Vision (ECCV)*, 2022.
- Hao Chen, Bo He, Hanyu Wang, Yixuan Ren, Ser Nam Lim, and Abhinav Shrivastava. Nerv: Neural representations for videos. *Advances in Neural Information Processing Systems*, 34:21557–21568, 2021a.
- Yinbo Chen, Sifei Liu, and Xiaolong Wang. Learning continuous image representation with local implicit image function. In *Proceedings of the IEEE/CVF conference on computer vision and pattern recognition*, pp. 8628–8638, 2021b.
- Julian Chibane, Thiemo Alldieck, and Gerard Pons-Moll. Implicit functions in feature space for 3d shape reconstruction and completion. In *Proceedings of the IEEE/CVF Conference on Computer Vision and Pattern Recognition*, pp. 6970–6981, 2020.
- Ekin D Cubuk, Barret Zoph, Jonathon Shlens, and Quoc V Le. Randaugment: Practical automated data augmentation with a reduced search space. In *Proceedings of the IEEE/CVF conference on computer vision and pattern recognition workshops*, pp. 702–703, 2020.
- Prafulla Dhariwal and Alexander Nichol. Diffusion models beat gans on image synthesis. *Advances in Neural Information Processing Systems*, 34:8780–8794, 2021.
- Alexey Dosovitskiy, Lucas Beyer, Alexander Kolesnikov, Dirk Weissenborn, Xiaohua Zhai, Thomas Unterthiner, Mostafa Dehghani, Matthias Minderer, Georg Heigold, Sylvain Gelly, Jakob Uszkoreit, and Neil Houlsby. An image is worth 16x16 words: Transformers for image recognition at scale. In *International Conference on Learning Representations*, 2021.
- Emilien Dupont, Adam Goliński, Milad Alizadeh, Yee Whye Teh, and Arnaud Doucet. Coin: Compression with implicit neural representations. *arXiv preprint arXiv:2103.03123*, 2021a.
- Emilien Dupont, Yee Whye Teh, and Arnaud Doucet. Generative models as distributions of functions. *arXiv preprint arXiv:2102.04776*, 2021b.
- Emilien Dupont, Hyunjik Kim, S. M. Ali Eslami, Danilo Rezende, and Dan Rosenbaum. From data to functa: Your data point is a function and you can treat it like one. In *ICML*, 2022a.
- Emilien Dupont, Hrushikesh Loya, Milad Alizadeh, Adam Goliński, Yee Whye Teh, and Arnaud Doucet. Coin++: Data agnostic neural compression. *arXiv preprint arXiv:2201.12904*, 2022b.

- 
- Sara Fridovich-Keil, Alex Yu, Matthew Tancik, Qinhong Chen, Benjamin Recht, and Angjoo Kanazawa. Plenoxels: Radiance fields without neural networks. In *CVPR*, 2022.
- David Ha. Generating large images from latent vectors. 2016. URL <https://blog.otoro.net/2016/04/01/generating-large-images-from-latent-vectors/>.
- Jonathan Ho and Tim Salimans. Classifier-free diffusion guidance. *arXiv preprint arXiv:2207.12598*, 2022.
- Jonathan Ho, Ajay Jain, and Pieter Abbeel. Denoising diffusion probabilistic models. In H. Larochelle and M. Ranzato and R. Hadsell and M.F. Balcan and H. Lin (ed.), *Advances in Neural Information Processing Systems*, volume 33, pp. 6840–6851, 2020.
- Chiyu Jiang, Avneesh Sud, Ameesh Makadia, Jingwei Huang, Matthias Nießner, Thomas Funkhouser, et al. Local implicit grid representations for 3d scenes. In *Proceedings of the IEEE/CVF Conference on Computer Vision and Pattern Recognition*, pp. 6001–6010, 2020.
- Tero Karras, Timo Aila, Samuli Laine, and Jaakko Lehtinen. Progressive growing of gans for improved quality, stability, and variation. In *International Conference on Learning Representations*, 2018.
- Subin Kim, Sihyun Yu, Jaeho Lee, and Jinwoo Shin. Scalable neural video representations with learnable positional features. *arXiv preprint arXiv:2210.06823*, 2022.
- Diederik P Kingma and Jimmy Ba. Adam: A method for stochastic optimization. *arXiv preprint arXiv:1412.6980*, 2014.
- Ilya Loshchilov and Frank Hutter. Fixing weight decay regularization in adam. 2017.
- Luca De Luigi, Adriano Cardace, Riccardo Spezialetti, Pierluigi Zama Ramirez, Samuele Salti, and Luigi di Stefano. Deep learning on implicit neural representations of shapes. In *ICLR*, 2023.
- Ishit Mehta, Michaël Gharbi, Connelly Barnes, Eli Shechtman, Ravi Ramamoorthi, and Manmohan Chandraker. Modulated periodic activations for generalizable local functional representations. In *Proceedings of the IEEE/CVF International Conference on Computer Vision*, pp. 14214–14223, 2021.
- Lars Mescheder, Michael Oechsle, Michael Niemeyer, Sebastian Nowozin, and Andreas Geiger. Occupancy networks: Learning 3d reconstruction in function space. In *Proceedings of the IEEE/CVF Conference on Computer Vision and Pattern Recognition*, pp. 4460–4470, 2019.
- Ben Mildenhall, Pratul P Srinivasan, Matthew Tancik, Jonathan T Barron, Ravi Ramamoorthi, and Ren Ng. Nerf: Representing scenes as neural radiance fields for view synthesis. In *European Conference on Computer Vision*, pp. 405–421, 2020.
- Thomas Müller, Alex Evans, Christoph Schied, and Alexander Keller. Instant neural graphics primitives with a multiresolution hash encoding. *ACM Trans. Graph.*, 41(4):102:1–102:15, July 2022.
- Alexander Quinn Nichol and Prafulla Dhariwal. Improved denoising diffusion probabilistic models. In *International Conference on Machine Learning*, pp. 8162–8171. PMLR, 2021.
- Jeong Joon Park, Peter Florence, Julian Straub, Richard Newcombe, and Steven Lovegrove. DeepSDF: Learning continuous signed distance functions for shape representation. In *Proceedings of the IEEE Conference on Computer Vision and Pattern Recognition*, pp. 165–174, 2019.
- Robin Rombach, Andreas Blattmann, Dominik Lorenz, Patrick Esser, and Björn Ommer. High-resolution image synthesis with latent diffusion models. In *Proceedings of the IEEE/CVF Conference on Computer Vision and Pattern Recognition*, pp. 10684–10695, 2022.
- David W. Romero, Robert-Jan Brintjes, Jakub Mikolaj Tomczak, Erik J Bekkers, Mark Hoogendoorn, and Jan van Gemert. Flexconv: Continuous kernel convolutions with differentiable kernel sizes. In *International Conference on Learning Representations*, 2022a.



- 
- David W. Romero, Anna Kuzina, Erik J Bekkers, Jakub Mikolaj Tomczak, and Mark Hoogendoorn. CKConv: Continuous kernel convolution for sequential data. In *International Conference on Learning Representations*, 2022b.
- Olaf Ronneberger, Philipp Fischer, and Thomas Brox. U-Net: Convolutional networks for biomedical image segmentation. In *Medical Image Computing and Computer-Assisted Intervention – MICCAI 2015*, pp. 234–241. Springer International Publishing, 2015.
- Jonathan Richard Schwarz and Yee Whye Teh. Meta-learning sparse compression networks. *arXiv preprint arXiv:2205.08957*, 2022.
- Liyue Shen, John Pauly, and Lei Xing. Nerp: implicit neural representation learning with prior embedding for sparsely sampled image reconstruction. *IEEE Transactions on Neural Networks and Learning Systems*, 2022.
- J Ryan Shue, Eric Ryan Chan, Ryan Po, Zachary Ankner, Jiajun Wu, and Gordon Wetzstein. 3d neural field generation using triplane diffusion. *arXiv preprint arXiv:2211.16677*, 2022.
- Vincent Sitzmann, Julien N P Martel, Alexander W Bergman, David B Lindell, and Gordon Wetzstein. Implicit neural representations with periodic activation functions. In *Advances in Neural Information Processing Systems*, volume 33, 2020.
- Andreas Peter Steiner, Alexander Kolesnikov, Xiaohua Zhai, Ross Wightman, Jakob Uszkoreit, and Lucas Beyer. How to train your ViT? data, augmentation, and regularization in vision transformers. *Transactions on Machine Learning Research*, June 2022.
- Yannick Strömpler, Janis Postels, Ren Yang, Luc Van Gool, and Federico Tombari. Implicit neural representations for image compression. In *Computer Vision–ECCV 2022: 17th European Conference, Tel Aviv, Israel, October 23–27, 2022, Proceedings, Part XXVI*, pp. 74–91. Springer, 2022.
- Christian Szegedy, Vincent Vanhoucke, Sergey Ioffe, Jon Shlens, and Zbigniew Wojna. Rethinking the inception architecture for computer vision. In *Proceedings of the IEEE conference on computer vision and pattern recognition*, pp. 2818–2826, 2016.
- Ashish Vaswani, Noam Shazeer, Niki Parmar, Jakob Uszkoreit, Llion Jones, Aidan N Gomez, Łukasz Kaiser, and Illia Polosukhin. Attention is all you need. In *Advances in neural information processing systems*, pp. 5998–6008, 2017.
- Clinton J Wang and Polina Golland. Deep learning on implicit neural datasets. *arXiv preprint arXiv:2206.01178*, 2022.
- Qiang Wang, Bei Li, Tong Xiao, Jingbo Zhu, Changliang Li, Derek F Wong, and Lidia S Chao. Learning deep transformer models for machine translation. In *Proceedings of the 57th Annual Meeting of the Association for Computational Linguistics*, pp. 1810–1822, 2019.
- Ruibin Xiong, Yunchang Yang, Di He, Kai Zheng, Shuxin Zheng, Chen Xing, Huishuai Zhang, Yanyan Lan, Liwei Wang, and Tiejun Liu. On layer normalization in the transformer architecture. In *International Conference on Machine Learning*, pp. 10524–10533. PMLR, 2020.

---

## A BACKGROUND ON FUNCTA

In this section we give a summary of the methodology used by Dupont et al. (2022a). Please refer to the original paper for more details.

*Functa* are used to describe neural fields  $f_\theta$  that should be thought of as data. In this work, each  $f_\theta$  is a SIREN (Sitzmann et al., 2020), namely an MLP with sine non-linearities, that is fit to a single image by minimizing reconstruction loss on all pixels. In order to perform deep learning tasks on this dataset of neural fields (*functaset*), we would like to represent each field (*functum*) with an array that can be used as an input to neural networks.

A naïve approach would be to use the parameter vector  $\theta$  of the MLP as the array-representation of the field, but this representation is likely unnecessarily high dimensional. A more economical approach would be to share parameters across different fields in order to amortize the cost of learning the shared structure across these fields, and model the variations with a lower dimensional, per-field representation that modulates the shared parameters. One can split the parameters as follows: share the weights of a base SIREN across all fields and then infer per-field biases or *shifts*. The concatenation of these bias terms across all SIREN layers is referred to as the *shift modulation* (see Fig. 1), which now serves as a more compact representation of each field. Dupont et al. (2022a) show that only adapting the biases is already sufficient to model the variations across different fields to high reconstruction accuracy.

One can further reduce the dimensionality of these field representations by having a latent vector  $z$  that is linearly mapped onto the shift modulation; the linear map is shared across all fields. These latents then serve as representations for various downstream deep learning tasks such as classification or generation used in Dupont et al. (2022a).

In order to learn the shared parameters (base SIREN and latent-to-modulation linear map) and the per-field representation  $z$ , Dupont et al. (2022a) propose to use meta-learning, namely a double-loop optimization procedure that minimizes the reconstruction loss on all pixels. Given a batch of  $B$  images, the inner loop initializes  $B$  copies of per-field latents  $z$  to zero, and updates each with three SGD steps with respect to the reconstruction loss. The outer loop updates the shared parameters with Adam (Kingma & Ba, 2014) to minimize the reconstruction loss using the inner-loop updated values of  $z$ , with gradients flowing through the inner loop. Dupont et al. (2022a) show that this allows one to effectively learn the shared parameters, after which the  $z$  for each field can be fit very fast using three SGD inner loop steps. They show that three steps is already sufficient to achieve high quality reconstructions. This is how a *functaset* is created from each dataset.

## B LIMITATIONS OF NAIVELY SCALING FUNCTA

### B.1 EXPERIMENTAL DETAILS FOR FUNCTA ON CIFAR-10

**Meta-learning** To create the CIFAR-10 *functaset* (original vector *functum*), we use the same hyperparameter configurations as the meta-learning used in Dupont et al. (2022a) on CelebA-HQ  $64 \times 64$  except for the total batch size. Namely, we use  $\omega_0 = 30$ , SIREN width 512, depth 15, outer learning rate  $3e-6$ , using meta-SGD, with total batch size 128. We use the same initializations for the SIREN weights and biases, meta-SGD learning rates, and a zero initialization of the latent  $z$ .

**Classification** We use the same classifier architecture as Dupont et al. (2022a), namely an MLP with SiLU/swish activations and dropout, and also test a vanilla Transformer (with positional encodings). We additionally use:

- Standard data augmentation with left/right flips and random crops (taking  $32 \times 32$  crops of a  $40 \times 40$  image obtained by padding zeros to the boundary of the original image), using 50 randomly sampled augmentations per training image to create the augmented *functaset*.
- Scalar normalizing factor to normalize the *functum* latents before feeding them into the classifier.
- Label smoothing (Szegedy et al., 2016) hyperparameter  $l$  such that e.g. the one hot label  $[1, 0, \dots, 0]$  for  $n$  classes is replaced with  $[1 - l + l/n, l/n, \dots, l/n]$ .

- Weight decay with AdamW (Loshchilov & Hutter, 2017).
- Track exponential moving average of parameters throughout training that is used at evaluation time, using decay rate 0.9999.

We performed a large hyperparameter sweep over normalizing factor in  $[0.01, 0.03, 0.1]$ , learning rate in  $[1e-4, 1e-3, 1e-2]$ , label smoothing  $l$  in  $[0, 0.1]$ , weight decay in  $[0, 1e-1]$ , dropout in  $[0, 0.1, 0.2]$ , MLP width in  $[128, 256, 512, 1024]$ , MLP depth in  $[2, 3, 4, 5]$ , Transformer width in  $[64, 128, 256]$ , Transformer depth in  $[2, 3, 4]$ , with Transformer ffw-width being double the width. All models were trained for 300k iterations on a batch size of 256, and we report the best test accuracy throughout training. The optimal performance was given by an MLP on 512-dimensional latents at 68.3% test accuracy with normalizing factor 0.01, learning rate  $1e-3$ , label smoothing 0.1, weight decay 0.1, dropout 0.2, width 1024, depth 3. The best performing Transformer was on 256-dimensional latents at 63.5% test accuracy with normalizing factor 0.1, learning rate  $1e-3$ , label smoothing 0.1, weight decay 0.1, dropout 0.1, width 256, depth 2.

**Generation with diffusion models** We use the same DDPM (Ho et al., 2020) architecture as Dupont et al. (2022a) with ResidualMLP blocks, following their hyperparameters configurations and sweeps as closely as possible: functa latents are mean centered and normalized by the elementwise mean and standard deviation across the training set, and Adam is used with a learning rate schedule that warms up linearly from 0 to  $3e-4$  for the first 4000 iterations, followed by inverse square root decay. We use a batch size of 128 and sweep over the width in  $[512, 1024, 2048, 4096]$ , number of blocks in  $[2, 4]$ , training for 1M iterations. The optimal performance was given by 256-dimensional latents at 78.2 FID with width 4096, number of blocks 2.

## B.2 FUNCTA RECONSTRUCTIONS ON CIFAR-10

In Sec. 3 we showed that naively scaling vector-valued functa (Dupont et al., 2022a) does not lead to representations that can be easily used for downstream tasks despite yielding high reconstruction PSNRs. In Fig. 3 we show original images from the CIFAR-10 test set as well as their high-quality reconstructions using vector-valued functa.



Figure 3: *Functa* with flat (vector) latent representations obtained through meta-learning can reconstruct test images to high fidelity. Compare the original CIFAR-10 test images (*left*) and their functa reconstructions (*right*).

## B.3 FUNCTA PERTURBATION ANALYSIS ON CIFAR-10

To show that the individual dimensions of the latent vector indeed affect the entire image (as opposed to local regions) we perform a simple perturbation analysis similar to Dupont et al. (2022a), see

Fig. 4. For a set of functa we perturb the same latent dimension and then observe the changes in the pixel space. As discussed in the main text, perturbing each latent dimension individually gives indeed rise to perturbations throughout the entire image.

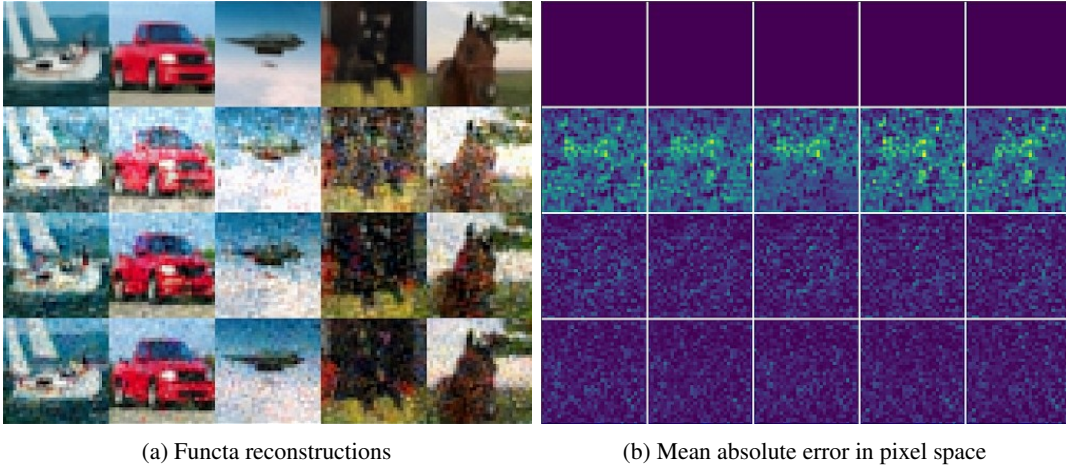


Figure 4: Perurbation of vector-valued functa on CIFAR-10. *Row 1*: unperturbed functa reconstructions. *Row 2*: perturbing latent dimension with largest mean absolute error in pixel space (MAE). *Row 3*: perturbing latent dimension with median MAE. *Row 4*: perturbing latent dimension with lowest MAE.

## C SPATIAL FUNCTA: EXPERIMENTAL DETAILS AND ADDITIONAL RESULTS

**Coordinate representation for SIREN** When using the *nearest neighbor* interpolation for spatial functa, where the  $c$ -dimensional latent feature vector at each spatial index represents an image patch, we found that using a per-patch coordinate representation as the input to the SIREN neural field helped optimization such that reconstructions achieve better PSNR values compared to a global coordinate representation. For example, for the bottom-left patch of size  $d/s \times d/s$ , we use coordinate representations  $\mathbf{x} \in [0, 1]^2$  rather than  $\mathbf{x} \in [0, s/d]^2$ . This allowed the meta-learning step to fit individual images to higher PSNR. For *linear* interpolation we empirically found that using a binary representation of the global coordinates gave better PSNR values than the patch-based coordinate representation above. For example, for CIFAR-10 at  $32 \times 32$  resolution, the coordinate at location  $(3/32, 5/32)$  would be converted to binary (00011, 00101), concatenated to 0001100101, then converted to a binary vector  $[0, 0, 0, 1, 1, 0, 0, 1, 0, 1]$ . Hence for an image of  $2^m \times 2^m$  resolution, we'd use a  $2m$ -dimensional binary coordinate representation. Although we did not try using the binary representation for *nearest neighbor* interpolation, we expect it to perform similarly to the per-patch coordinate representation.

**Classification** We use the standard vanilla pre-LN Transformer (Vaswani et al., 2017; Wang et al., 2019; Xiong et al., 2020) with absolute positional encodings where each input token is the  $c$ -dimensional latent feature vector of the spatial functa at each spatial index. Hence the sequence length of the Transformer is  $s^2$  where each spatial functa is given by latent  $\mathbf{z} \in \mathbb{R}^{s \times s \times c}$ . Similar to classification experiments on the original vector-valued functa in App. B.1, we use data augmentation, scalar normalization of input latents, label smoothing and weight decay. Dropout is only applied once just before the final linear layer that maps onto the logits. For CIFAR-10, we use the same random crop and flip augmentations, whereas for ImageNet we use random distorted bounding box crops and flips (following Szegedy et al. (2016)) followed by RandAugment (Cubuk et al., 2020) with 2 sequential augmentations at magnitude 5.

**Generation with diffusion models** We closely follow the improved implementation of discrete-time denoising diffusion probabilistic models (DDPMs) (Ho et al., 2020) by Dhariwal & Nichol (2021), and optionally use classifier-free guidance (Ho & Salimans, 2022) for generation. We use 1000 diffusion time steps and a cosine noising schedule and train the denoising model using the

original (simplified) DDPM loss though we also explored non-uniform sampling distributions for the time steps. Our denoising architecture is the same UNet (Ronneberger et al., 2015) used by Dhariwal & Nichol (2021) and we use the  $\epsilon$  (noise prediction) parameterization, which we found to work best.

### C.1 EXPERIMENTAL DETAILS FOR CIFAR-10

**Meta-learning** For meta-learning, we sweep over the below hyperparameters to find the ones that give optimal PSNR on the test set, using  $\omega_0 = 10$ , batch size 128, 200k training iterations for  $8 \times 8$  spatial latent dimensions and 500k iterations for  $4 \times 4$  spatial latent dimensions:

latent shape	interpolation	SIREN width	SIREN depth	outer learning rate
$8 \times 8 \times 16$	1-NN	256	6	3e-5
$8 \times 8 \times 16$	linear	256	6	1e-4
$4 \times 4 \times 64$	1-NN	256	10	3e-5
$4 \times 4 \times 64$	linear	256	10	3e-5

Table 4: Optimal hyperparameter configuration for meta-learning on CIFAR-10

**Classification** We sweep over the below hyperparameters to find the ones that give optimal test accuracy, using label smoothing 0.1, weight decay 0.1, 16 Transformer heads, for 100k training iterations, see Tab. 5.

latent shape	interpolation	normalization scale	Transformer width	ffw width	number of blocks	learning rate	dropout rate	batch size
$8 \times 8 \times 16$	1-NN	0.08	128	256	12	1e-2	0.1	256
$8 \times 8 \times 16$	linear	0.1	128	256	12	1e-2	0.2	256
$4 \times 4 \times 64$	1-NN	0.01	384	768	12	2e-3	0.1	512
$4 \times 4 \times 64$	linear	0.01	384	768	16	2e-3	0.2	512

Table 5: Optimal hyperparameter configuration for classification on CIFAR-10

**Generation** For generation with diffusion models we swept over several architecture and noising hyperparameters to determine the best configuration for each latent space shape and interpolation based on FID. We trained for 500k iterations using a batch size of 256 and learning rate  $10^{-4}$  using Adam with default parameters, dummy-label proportion of 0.2 for classifier-free guidance. We used vector-valued normalization and tune the scale factor (see App. C.4.1). See Tab. 6 for the optimal hyperparameters in terms of the denoising architecture.

### C.2 ASSESSING MEMORIZATION ON CIFAR-10

In Sec. 5.1 we mentioned that class-conditional diffusion models can overfit on CIFAR-10 by memorizing a subset of the training data; i.e. at sampling time the model only produces samples from this subset. Here, we discuss this in more detail.

We assessed memorization by finding the closest training set image (in pixel-space) to each model sample, see Fig. 5 for examples. We found that diffusion models with class-conditional UNets of different sizes perfectly memorized a subset of the training data, see Fig. 5(b). While Nichol & Dhariwal (2021) found that using a suitable dropout rate in the UNet allowed for a good trade-off between sample quality and overfitting for diffusion on pixel space, we were unable to find such a trade-off for our models – they overfit even with strong dropout or yielded low-quality samples. Instead, we found that using unconditional models provided a better trade-off, see Fig. 5(a).

Despite memorizing training examples almost perfectly with class-conditional models, we still observe a relatively large FID of  $\sim 10$ . Below we show that this is due to mode dropping; i.e., the

conditional	latent shape	interpolation	normalization scale		noising schedule		# res blocks	channels	channel multiplier	attention res	dropout rate
✗	$8 \times 8 \times 16$	1-NN	2	linear	1	320	(1, 1)	(4, )	0.4		
✗	$8 \times 8 \times 16$	linear	2	cosine	2	320	(2, 2)	(2, )	0.4		
✗	$4 \times 4 \times 64$	1-NN	2	cosine	2	320	(2, 2)	—	0.4		
✗	$4 \times 4 \times 64$	linear	2	cosine	2	320	(2, 2)	(4, )	0.4		
✓	$8 \times 8 \times 16$	1-NN	2	cosine	3	320	(2, 2, 2)	(8, )	0.1		
✓	$8 \times 8 \times 16$	linear	2	cosine	3	320	(2, 2, 2)	(8, 4, )	0		
✓	$4 \times 4 \times 64$	1-NN	2	cosine	3	320	(2, 2)	(4, )	0		
✓	$4 \times 4 \times 64$	linear	2	cosine	3	320	(2, 2, 2)	(4, 2)	0		

Table 6: Optimal hyperparameter configuration for diffusion models on CIFAR-10. Note that all conditional models overfit and memorize a subset of the training set, see [App. C.2](#).

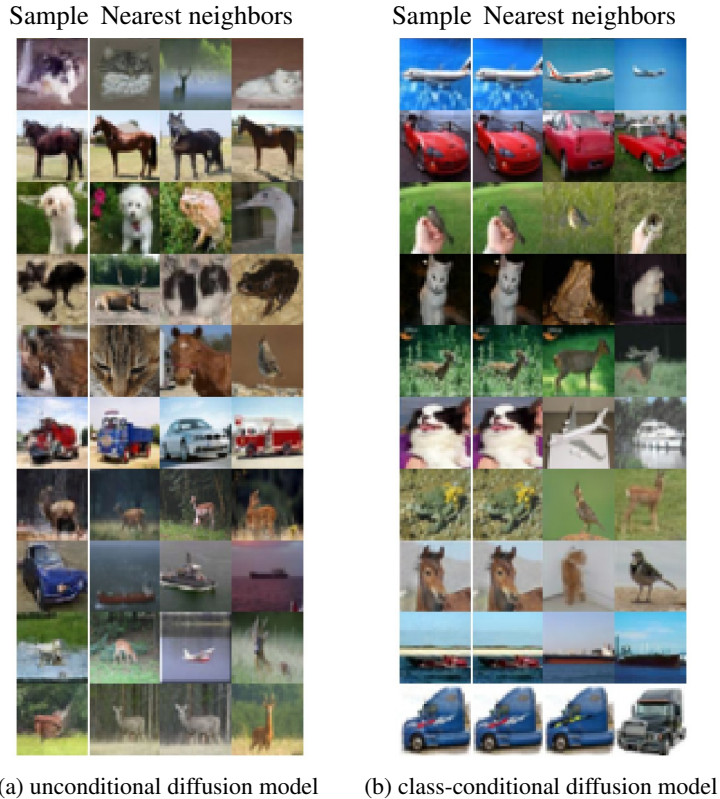


Figure 5: Assessing memorization of CIFAR-10 training set. For each sample we show the three nearest neighbors (in pixel-space) from the training set.

model does not memorize the entire training set but only a subset, thus not matching the covariance of the training data used for the FID evaluation.

We sampled 5000 images per class from the model and looked up their nearest neighbors in the training set. We also verified that each sample indeed corresponded to a very close example in the training set. We then counted the number of *distinct* samples per class such found. If the model perfectly remembered the training data, it should produce each image of a particular class from the training set with the same probability ( $1/5000$  in the case of the CIFAR-10). The expected number of distinct samples when sampling 5000 images from the class would then be 3161 (with a standard deviation of 34); this corresponds to drawing 5000 times i.i.d. from a set of 5000 distinguishable

objects *with* replacement and asking how many unique objects we would draw. We find that the overfitting models produce significantly fewer unique samples, see Tab. 7. This corresponds to mode dropping, i.e. memorization of only a subset of the training images, or at least sampling them with very uneven probabilities.

expected	observed (class number)									
	(1)	(2)	(3)	(4)	(5)	(6)	(7)	(8)	(9)	(10)
3161	1219	1927	1800	1904	1547	1437	1492	1644	1555	1842

Table 7: Counts of unique images memorized from the training set for each class vs the expected number if samples were drawn i.i.d. with replacement when sampling 5000 times.

### C.3 EXPERIMENTAL DETAILS FOR IMAGENET $256 \times 256$

For ImageNet-1k  $256 \times 256$ , we show the hyperparameter configurations for the spatial functa that give the best classification performance and those that give the best generation performance.

**Meta-learning** We use the following hyperparameter configurations for each of these latent shapes and choice of interpolation:

latent shape  $16 \times 16 \times 128$ , 1-NN interpolation: batch size 16, 500k training iterations, SIREN width 256, depth 12,  $\omega_0 = 20$ , outer learning rate  $1e-5$ .

latent shape  $32 \times 32 \times 64$ , 1-NN interpolation, using  $3 \times 3$  Conv for latent to modulation mapping: batch size 16, 500k training iterations, SIREN width 256, depth 8,  $\omega_0 = 10$ , outer learning rate  $3e-5$ .

**Classification** The following hyperaparameters gave the best classification results for latent shape  $16 \times 16 \times 128$ : label smoothing 0.1, weight decay 0.2, 200 training epochs, scalar normalization 0.005, learning rate  $1e-3$ , dropout 0.2, batch size 1024, Transformer width 768, ffw width 1536, number of blocks 18, 16 heads.

**Diffusion** The following hyperaparameters gave the best FID score for latent shape  $32 \times 32 \times 64$ : 1.5M training iterations, batch size 256, learning rate  $1e-4$ , dummy-label proportion 0.2, vector-valued normalization with scale factor 2.5, no dropout, cosine noising schedule, 2 residual blocks, channels 320, channel multiplier (1, 2, 2, 2), attention resolutions (8, 16).

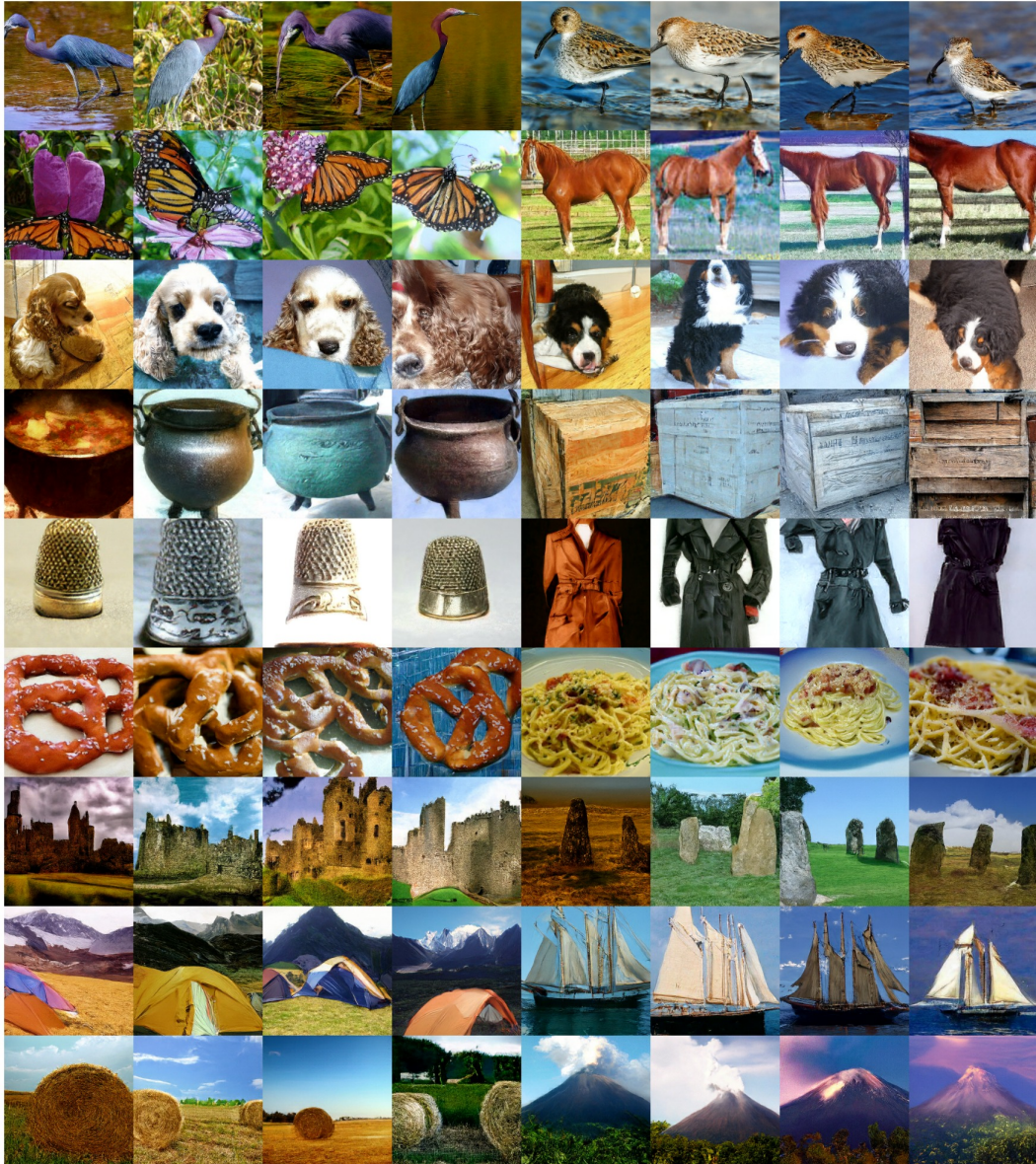


Figure 6: Uncurated ImageNet  $256 \times 256$  samples at guidance scale=5 for different classes from the best diffusion model trained on spatial functa.



## C.4 ABLATIONS

Apart from model size and latent shapes several other design decisions strongly impacted model performance, in particularly for image generation. These include the normalization of the functaset, the guidance scale for classifier-free guidance, and the sampling of timesteps for diffusion training. Here we present ablations for these choices and evaluate how they affect the FID score for diffusion modeling on spatial functa for ImageNet-1k  $256 \times 256$ .

### C.4.1 NORMALIZATION OF THE FUNCTASET PRIOR TO GENERATIVE MODELING

First, we investigate the normalization of the functaset before using them for downstream tasks. A priori the spatial latents  $z \in \mathbb{R}^{s \times s \times c}$  are unconstrained, however we find that they are confined to small values, most likely due to the 3-gradient-step meta-learning procedure. In Fig. 8 we display the means and standard deviations of the latent feature dimensions of a spatial functaset with  $s = 32, c = 64$  on ImageNet-1k ( $256 \times 256$ ). In the figure we average over the spatial dimensions as well as over examples.

In general, we find that the distribution of the meta-learned functaset is non-Gaussian and can have heavy tails, hence we choose to standardize the mean and standard deviation of the latents to simplify the generative modeling task of the diffusion model. We find that the choice of normalization has a strong effect on the final performance. We standardize the latents as

$$\tilde{z} = \frac{z - \mu}{\gamma \cdot \sigma} \tag{1}$$

where subtraction and division are element-wise and  $\mu$  and  $\sigma$  are means and standard deviations across the training set. In addition,  $\gamma$  denotes an additional (global) scale factor that we treat as a tunable hyperparameter.

We consider three different choices how to compute these means and standard deviations:

1. scalar-valued  $\mu, \sigma \in \mathbb{R}$ : compute means and standard deviations over all latent dimensions  $s \times s \times c$ ; each latent dimension is centred and scaled in the same way.
2. vector-valued  $\mu, \sigma \in \mathbb{R}^c$ : compute means and standard deviations over the spatial dimensions  $s \times s$ , but each of the  $c$  feature dimensions is centred and scaled independently of each other.
3. array-valued  $\mu, \sigma \in \mathbb{R}^{s \times s \times c}$ : compute means and standard deviations only across examples, and each of the latent dimensions  $s \times s \times c$  is treated independently of each other.

We find that vector- and array-normalization yield very similar results while scalar-normalization is markedly worse. Moreover, we find that a scale factor  $\gamma \approx 2.5$  yields the best results on ImageNet-256 empirically, see Fig. 7.

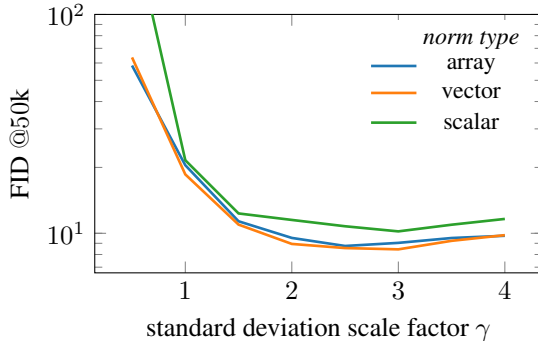


Figure 7: Ablation: Effect of different normalization types and scaling parameters used in normalizing the modulation latents for generative modeling.

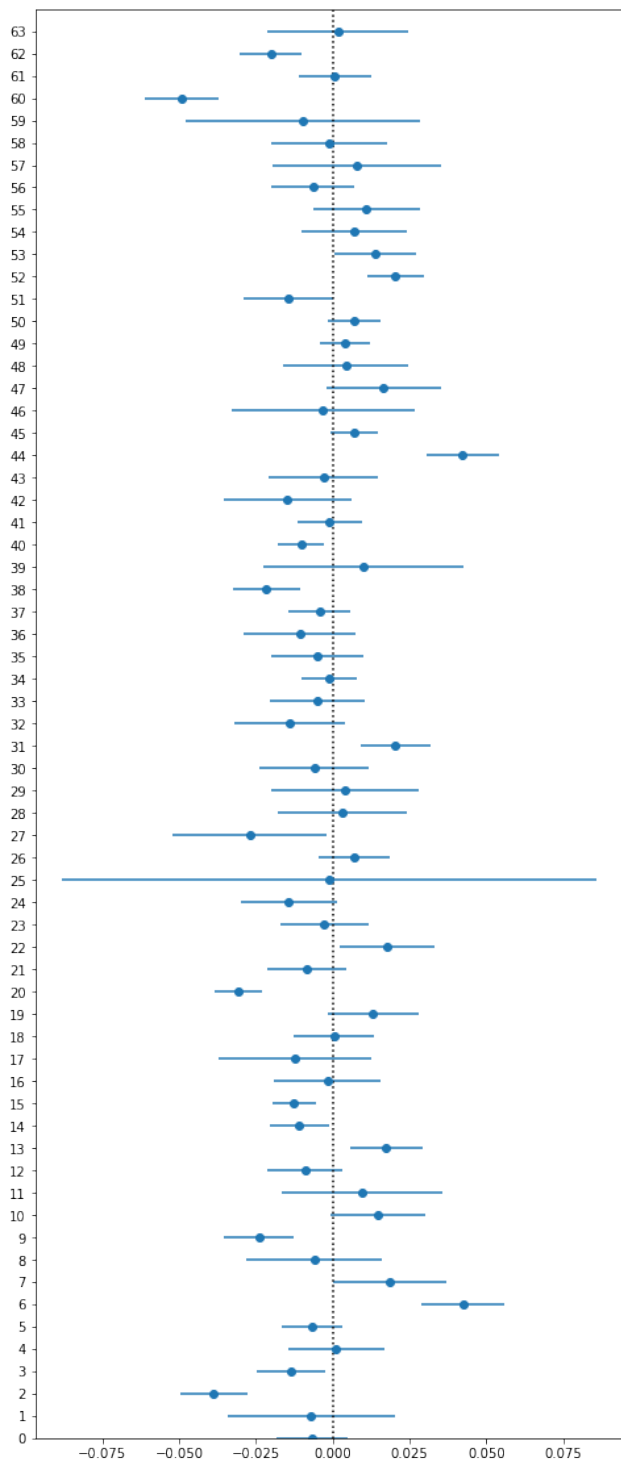


Figure 8: Mean and standard deviation of the 64 latent feature dimensions of a functaset with spatial latents  $32 \times 32 \times 64$  for ImageNet-1k  $256 \times 256$ . We compute the mean and standard deviation across spatial locations as well as examples.

### C.4.2 GUIDANCE SCALE

When sampling diffusion samples, we use classifier-free guidance (Ho & Salimans, 2022) to improve the image quality. In this ablation, we sweep the guidance scale for ImageNet-1k  $256 \times 256$  and find that the optimal guidance scale is between 4 and 5, see Fig. 9 (top). This range is larger than the range typically found for diffusion modeling in pixel space (Ho & Salimans, 2022) or latent space (Rombach et al., 2022). In all our experiments in the main paper we use classifier-free guidance with a guidance scale of 5. In Fig. 9 (bottom) we show uncurated samples for different classes and for different values of the guidance scale. Too small guidance scales lead to unclear samples whereas too large guidance scales lead to patch boundary artifacts or exaggerated contrast.

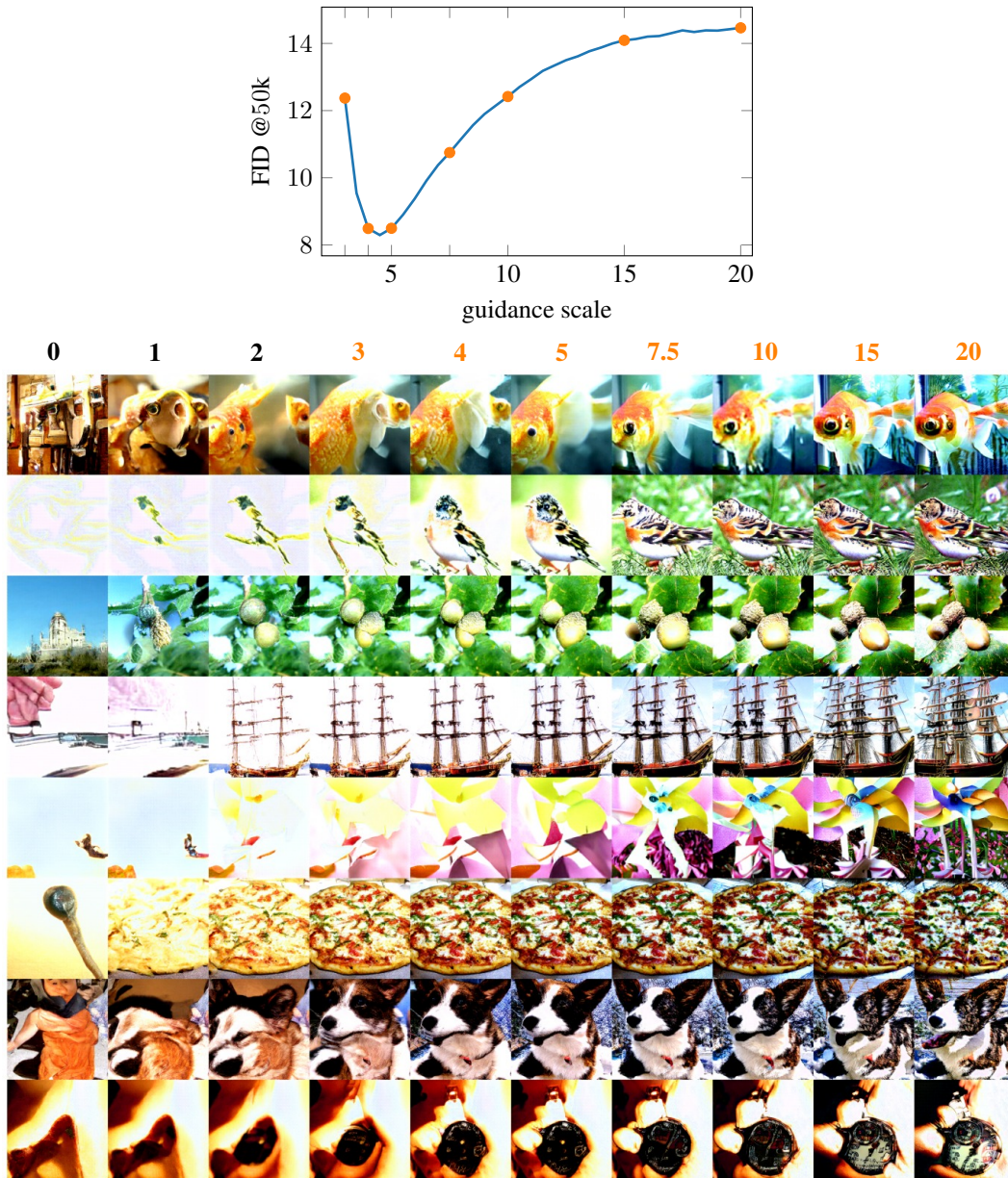


Figure 9: Class-conditional classifier-free DDPM sampling from a diffusion model at different guidance scales ranging from 0 (unconditional samples) to 20. *Top*: FID values using 50k samples; *bottom*: uncurated samples at different guidance scales. The orange dots in the upper plot correspond to the orange colored guidance scales  $\geq 3$ .

### C.4.3 RATIO OF TIME STEP SAMPLING DURING DIFFUSION TRAINING

For generative diffusion modeling we use the discrete-time formulation of diffusion models (DDPM) (Ho et al., 2020). While their simple training objective suggests to sample time-steps uniformly during training,  $t \sim \text{Uniform}(0, T)$ , we found that sampling earlier time steps more frequently lead to improved performance. We sample timesteps according to a distribution that linearly interpolates between a maximal probability value for timesteps  $t \rightarrow 0$  and a minimal value for timesteps  $t \rightarrow T$ . In Fig. 10 we vary the ratio between these two extremes ranging from 1 (uniform) to 7. We found that using a ratio of  $\geq 3$  gave the best results.

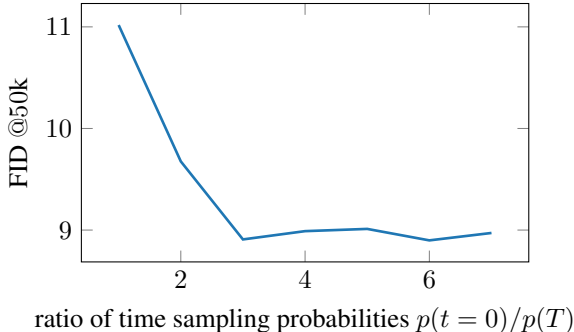


Figure 10: Ablation: Effect of sampling diffusion time steps with varying frequencies during training. A ratio of 1 corresponds to uniform sampling.

### C.4.4 QUANTIZATION

We show that spatial functa are highly compressible, making them amenable to neural-field based compression methods described in e.g. Dupont et al. (2021a; 2022b); Strümpfer et al. (2022); Schwarz & Teh (2022). In Fig. 11, we show that naïve uniform quantization of each 32 bit latent dimension of spatial functa leads to hardly any decrease in reconstruction quality down to 6 bits per dimension. In Tab. 8 we further show FID scores of class-conditional diffusion models trained on each of the quantized modulations, showing that there is hardly a loss in perceptual quality of samples down to 6 bits.

Num bits per latent dimension	32 (unquantized)	8	7	6
FID@50k (cond)	$8.7 \pm 0.2$	$9.0 \pm 0.2$	$8.8 \pm 0.2$	$9.2 \pm 0.1$

Table 8: ImageNet  $256 \times 256$  diffusion ablation on different levels of uniformly quantized spatial functa. We show means and standard deviations of FID scores over 3 random seeds.

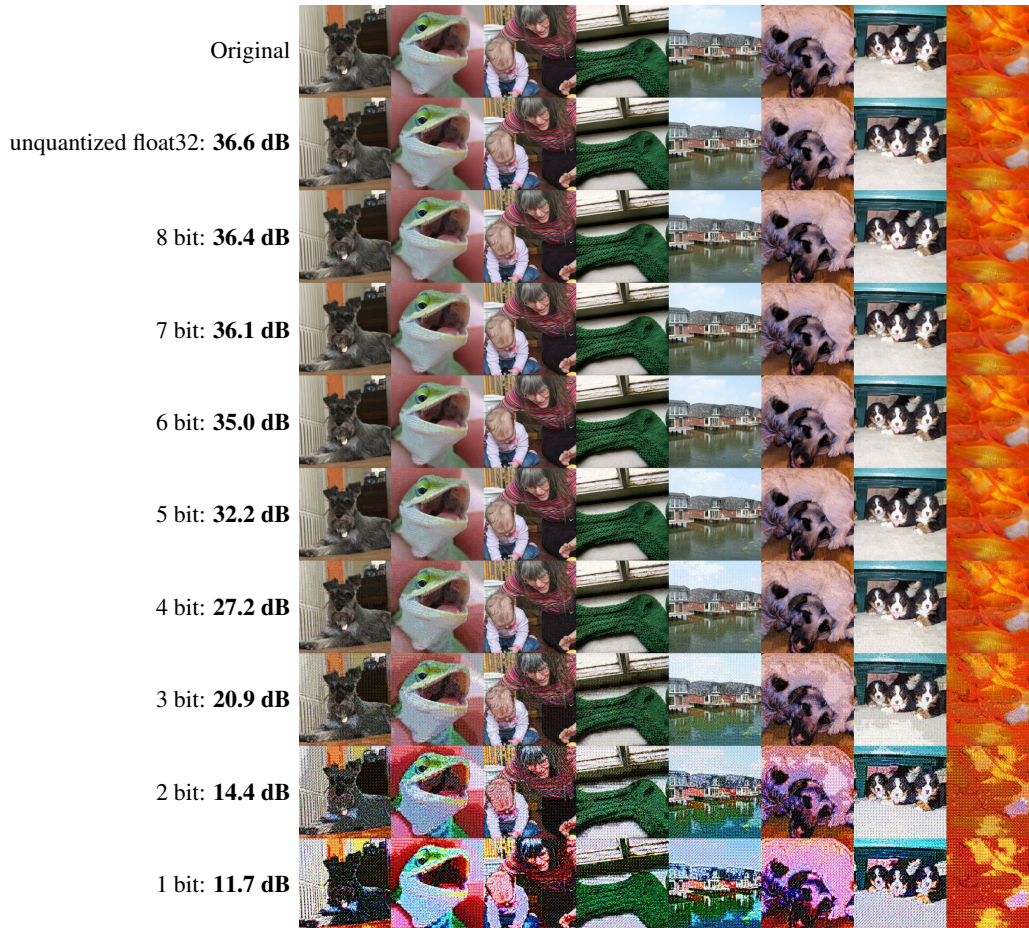


Figure 11: PSNR of different quantization levels for spatial functa shape  $32 \times 32 \times 64$  on ImageNet  $256 \times 256$  reconstructions. Quantization is per latent dimension, binning each into  $2^{\#bits}$  uniform bins. Best viewed zoomed in.

---

## C.5 PERTURBATION ANALYSIS OF SPATIAL FUNCTASETS

Here, we provide a brief perturbation analysis on spatial functa, similar to the analysis performed by Dupont et al. (2022a) as well as that presented in Fig. 4.

In our experiments, we perturbed individual feature dimensions at each spatial location of the  $s \times s$  spatial functa latent by the same constant value, see Fig. 12 for an example where we perturb the 26th (among the  $c = 64$ ) feature dimension at each spatial location for two images from ImageNet-1k ( $256 \times 256$ ). We observed that the difference between the original and perturbed image has a repeating pattern of size  $d/s$ , where  $d$  is the image size in pixels and  $s$  is the latent size. We found that the pattern is stable across patches of the same image as well as between images; thus, each latent feature dimension explains the same local feature in each patch. Note that the patterns are somewhat modulated in darker or brighter regions where the pixel values saturate. As the strength of the perturbation varies, so does the strength of the pattern. To some degree we can think of each feature dimension as coefficients of basis functions in the pixel space, though we only inspect perturbations of individual dimensions.

We further analyze how the strength of the pattern changes as we vary the strength of the perturbation. In Fig. 8 we saw that the typical range of the latent modulations is  $\leq 0.1$ ; we therefore explore perturbations with a strength in the range  $[-0.2, 0.2]$ . Like in Fig. 12 we perturb each of the  $c = 64$  feature dimension separately but at each of the  $s \times s = 32 \times 32$  spatial dimensions simultaneously. In Fig. 13 we show the average RMSE for each of the  $c = 64$  feature dimensions computed over  $8 \times 8$  patches (corresponding to the repeating pattern in Fig. 12) and images. Interestingly, we observe that for all of the  $c = 64$  feature dimensions the RMSE ( $y$ -axes) increases approximately linearly with the perturbation strength ( $x$ -axes). These preliminary results hint at the possibility that the latent feature dimensions encode coefficients of a set of linear basis functions, though further work in this direction is needed for verification.

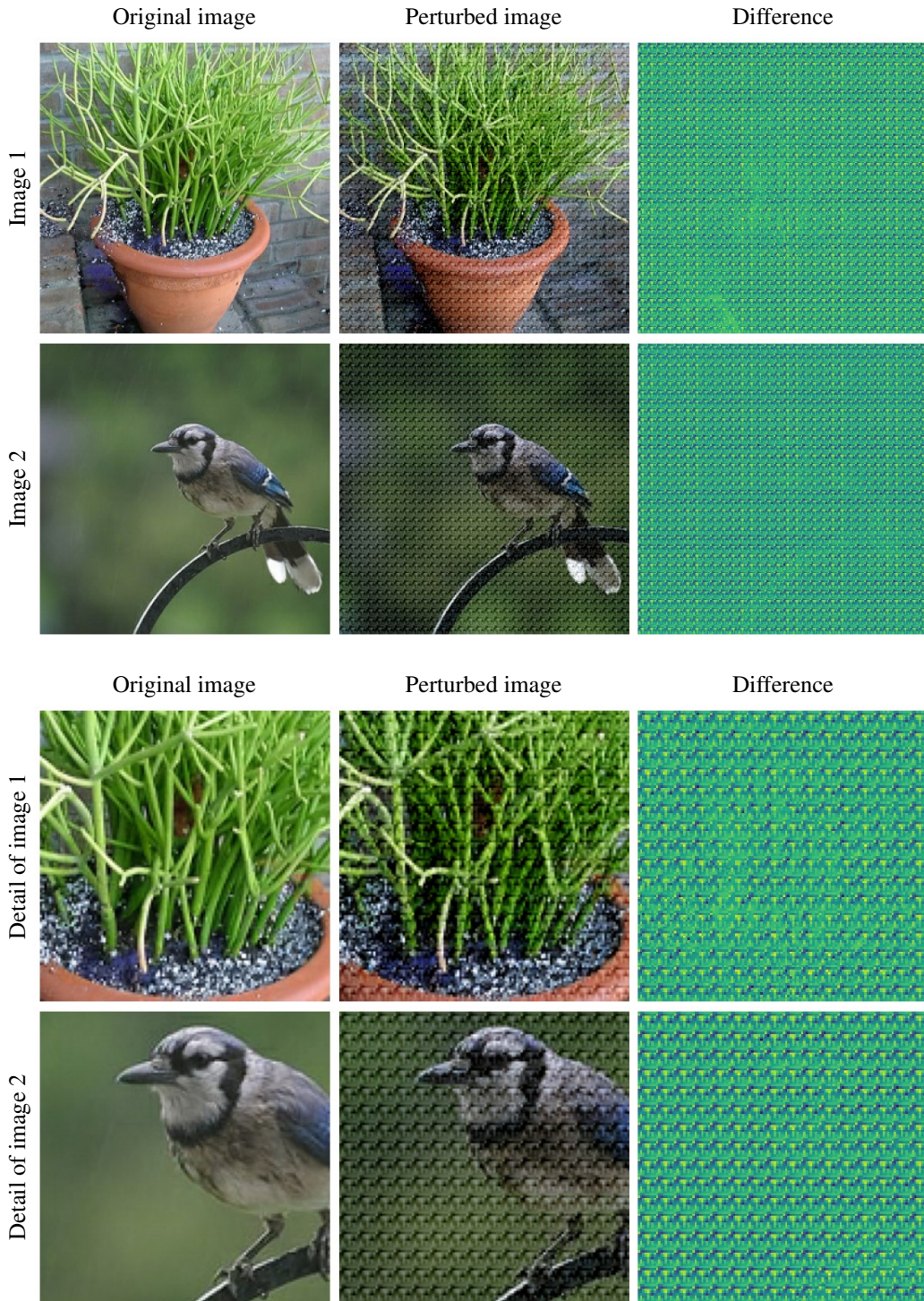


Figure 12: Example of a spatial functa perturbation. Here, we perturb the 26th feature dimension of every  $s \times s$  spatial latent by adding the same constant value to each while keeping all other feature dimensions unmodified. *top*: full  $256 \times 256$  image; *bottom*: zoomed in detail

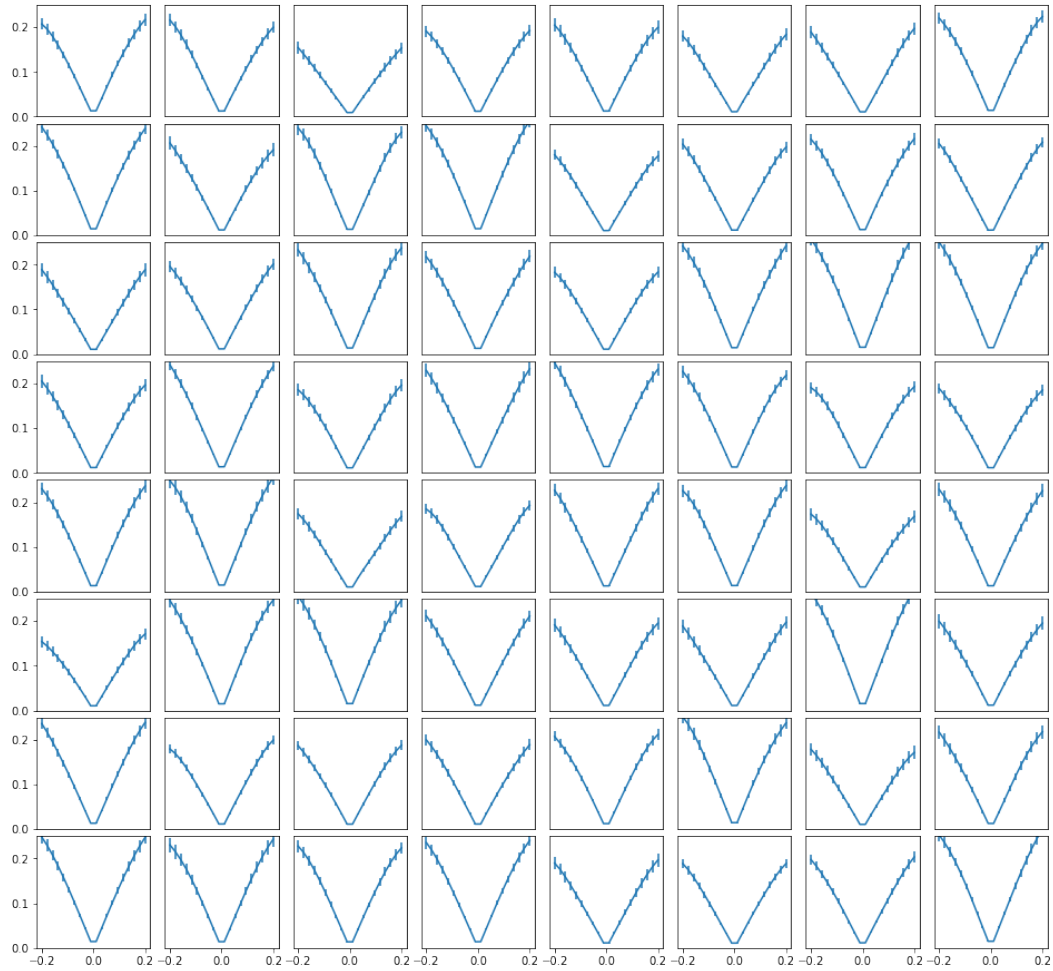


Figure 13: Perturbation analysis when independently perturbing each of the 64 feature dimension of every spatial latent by adding the same constant value to each while keeping all other feature dimensions unmodified. Each plot corresponds to one of the 64 feature dimensions. In each plot, the  $x$ -axis denotes the perturbation strength and the  $y$ -axis corresponds to the RMSE between the perturbed images and the original image.